The Generalized Contrast-to-Noise Ratio: A Formal Definition for Lesion Detectability

Alfonso Rodriguez-Molares, Ole Marius Hoel Rindal, *Student Member, IEEE*,
Jan D'hooge, *Member, IEEE*, Svein-Erik Måsøy, *Member, IEEE*,
Andreas Austeng, *Senior Member, IEEE*, Muyinatu A. Lediju Bell, *Senior Member, IEEE*,
and Hans Torp, *Member, IEEE*

Abstract— In the last 30 years, the contrast-to-noise ratio (CNR) has been used to estimate the contrast and lesion detectability in ultrasound images. Recent studies have shown that the CNR cannot be used with modern beamformers, as dynamic range alterations can produce arbitrarily high CNR values with no real effect on the probability of lesion detection. We generalize the definition of CNR based on the overlap area between two probability density functions. This generalized CNR (gCNR) is robust against dynamic range alterations; it can be applied to all kind of images, units, or scales; it provides a quantitative measure for contrast; and it has a simple statistical interpretation, i.e., the success rate that can be expected from an ideal observer at the task of separating pixels. We test gCNR on several state-of-the-art imaging algorithms and, in addition, on a trivial compression of the dynamic range. We observe that CNR varies greatly between the state-of-the-art methods, with improvements larger than 100%. We observe that trivial compression leads to a CNR improvement of over 200%. The proposed index, however, yields the same value for compressed and uncompressed images. The tested methods showed mismatched performance in terms of lesion detectability, with variations in gCNR ranging from -0.08 to $+0.29$. This new metric fixes a methodological flaw in the way we study contrast and allows us to assess the relevance of new imaging algorithms.

Index Terms— Contrast, detection, lesion, probability, ultrasound.

I. INTRODUCTION

THE concepts of contrast and lesion detection have been entwined since the early days of medical ultrasound. Back in the era of hardware beamforming, higher contrast meant easier detection of anatomical and pathogenic features. This relation was further studied and quantified in the seminal study by Smith *et al.* [1]. As a result, contrast and lesion detectability became synonymous in 1983.

However, it has been recently shown [2] that modern beamformers can alter the dynamic range of ultrasonic images and said alterations can, in turn, induce a fictitious increase of the measured contrast. As a consequence, a search for better contrast estimators has been called out [2].

This challenge extends beyond the problem of dynamic range alterations. Initially, in the hardware beamforming era, ultrasound images were, in essence, the maps of the backscattered wave intensity. However, contemporary ultrasound images can convey very different types of information, such as signal coherence [3]–[5], tissue elasticity [6]–[8], viscoelasticity [9], nonlinear elasticity [10], specularity [11], or even a combination of several heterogeneous parameters.

This new landscape raises some standing questions. How can we compute contrast across different methods? Should we use the same expressions to compute it? Should we use the same units? These questions are probably the cause for the variety of metrics found in the literature and the lack of consensus regarding which methods produce a higher probability of lesion detection.

This article tackles these questions and proposes a new metric, the generalized contrast-to-noise ratio (gCNR), that is, a surrogate of the maximum probability of success $P_{\max}$ of classic detection theory. We show that gCNR can be estimated in the same imaging scenarios as the classic CNR [12]. We hypothesize that contrary to CNR, gCNR is resistant to dynamic range alterations, can be used on any kind of data, regardless of the signal nature or units, and is a quantitative metric with a simple statistical interpretation.

This article is organized as follows. Section II revises the classic contrast metrics and illustrates how they break down if the dynamic range is altered. In Section III, we show how to estimate gCNR and derive an analytical expression for gCNR for delay-and-sum (DAS) in a standard anechoic phantom. Section IV describes the *in silico*, *in vitro*, and *in vivo* data used to demonstrate gCNR and briefly describes the state-of-the-art imaging methods that have been tested. In Section V, expressions are validated *in silico* and *in vitro*, the robustness of gCNR against dynamic range alterations is demonstrated, and the gCNR of the studied imaging methods is evaluated.

The use of gCNR on *in vivo* data is also illustrated in Section V. Results are discussed in Section VI, and concluding remarks are included in Section VII.

II. BACKGROUND

A. Classic Metrics

Let us define a lesion, such as a cyst embedded in a background area. Let us denote I as an area inside the lesion and O as an area outside the lesion. Let us denote any quantity computed within each region with the subindexes i and o, respectively.

The most popular measure of contrast in ultrasound imaging, often referred to simply as contrast, was already in use in 1985 [13]

$$C = \frac{\mu_i}{\mu_o} \quad (1)$$

where

$$\mu_i = E\{|s_i|^2\} \quad (2)$$
$$\mu_o = E\{|s_o|^2\} \quad (3)$$

are, respectively, the mean signal powers inside and outside the lesion, and s denotes the signal. Contrast can take any positive real value, and $C \to \infty$ as $\mu_o \to 0$. Contrast is often expressed in decibels as

$$C[dB] = 10 \log_{10} C. \quad (4)$$

An alternative measure of contrast, later known as the CNR, was introduced in 1983 by Patterson and Foster [12]

$$CNR = \frac{|\mu_i - \mu_o|}{\sqrt{\sigma_i^2 + \sigma_o^2}} \quad (5)$$

where

$$\sigma_i^2 = E\{(|s_i|^2 - \mu_i)^2\} \quad (6)$$
$$\sigma_o^2 = E\{(|s_o|^2 - \mu_o)^2\} \quad (7)$$

are, respectively, the variance of the signal power inside and outside the lesion. CNR can take any positive value, and $CNR \to \infty$ when $\sigma_i^2 + \sigma_o^2 \to 0$. For DAS, both speckle signal and thermal noise follow a circularly symmetric Normal distribution $\mathcal{CN}(0, \Gamma)$ [14], meaning that as shown in Section III-C, the CNR of DAS is bounded to the interval [0,1].

B. Other Metrics

Simultaneously, with [12], Smith *et al.* [1] proposed a lesion contrast metric based on a theoretical analysis of contrast-detail detectability for an ideal observer

$$CNR\dagger = \frac{|\mu_i - \mu_o|}{\sqrt{\mu_i^2 + \mu_o^2}} \quad (8)$$

which is similar to Patterson–Foster's CNR. In [1], the analysis is constructed upon the assumption that the signal power, both inside and outside lesion regions, follows an exponential distribution. Under that condition, the variance of the signal power equals its squared mean $\sigma^2 = \mu^2$, and (5) becomes equivalent to (8).

Even though (5) and (8) were conceived to be used with signal power in natural units, many authors have inserted log-compressed values in them [15]–[18]. This practice can be defended from an image processing perspective since, in many cases, detection is carried out on pixel intensity (in dB), not signal power, and hence, μ and σ^2 should be defined as the mean and variance of the pixel intensity. However, arbitrarily large values (CNR≫1) are achieved, which raises questions on the significance of those numeric values.

C. Obsolescence of the Classic Contrast Metrics

The classic definitions, (1), (5), and (8) have become obsolete due to the following reasons.

1) Some imaging algorithms do not produce an estimation of the tissue backscattering intensity, but something else. For example, short-lag-spatial coherence (SLSC) [19] produces images of the signal coherence, often displayed in the natural scale [20]. The same can be argued of other coherence-based algorithms [3], [5], [21].
2) It has been shown that adaptive algorithms can alter the statistics of the speckle signal [22] and the dynamic range of the beamformed signal [2]. This hinders the comparison of the metrics of different algorithms. To illustrate this, Fig. 1 shows two ultrasound images produced with DAS: Fig. 1(a) shows conventional DAS, and Fig. 1(c) shows the same data after being transformed using the S-curve in Fig. 1(b). In Fig. 1(a), we obtain a CNR = 0.8920, while in Fig. 1(c), CNR = 2.2887. Dynamic range transformations, such as the S-curve shown in Fig. 1(b), do not have a positive impact on lesion detection. At best, they leave the detection probability unaltered. In effect, if one calculates the detection probability, using the gCNR as described in this article, one finds that in both cases, it is 96.9%. It follows that higher CNR values do not necessarily imply a higher probability of lesion detection.
3) Often C and CNR improvements are estimated on trivial lesions, i.e., lesions that are already perfectly separable in the reference image. From a medical perspective, increasing the contrast of already detectable lesions is of little clinical value.

We ought to define a quality metric for lesion detectability that overcomes these three problems.

III. THEORY

It can be argued that CNR is correlated with the detection probability under certain conditions. A detection problem can be posed as a classification problem, where the percentage of pixels that are correctly classified is the detection probability.

In classification problems, the concept of maximum probability of success P_{max} is often used, defined as the maximum performance that can be expected from a classifier using a set of optimal thresholds. The complementary probability $P_{min} = 1 - P_{max}$ is known as the minimum probability of error.
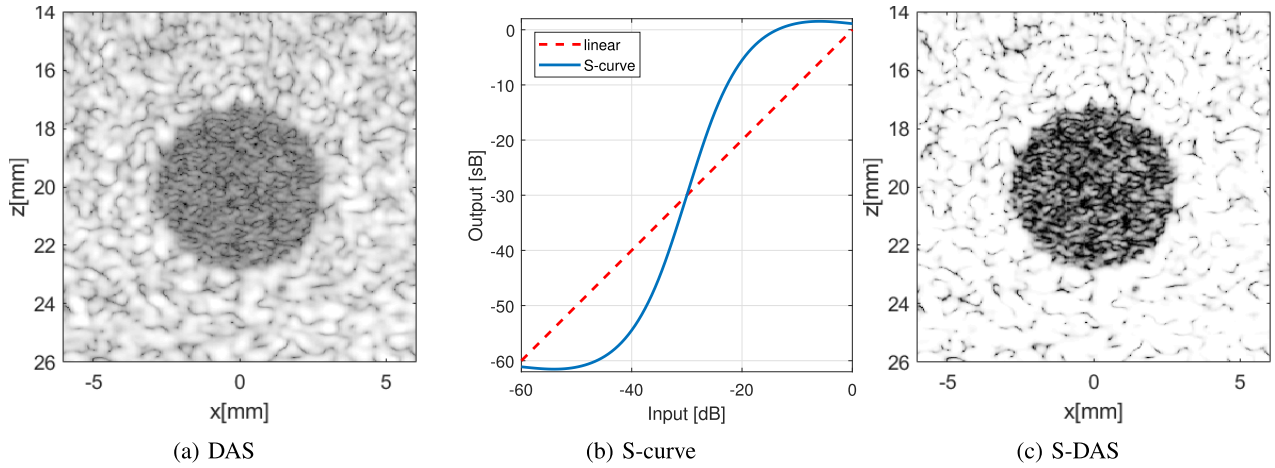
Fig. 1. Evidence that S-compression alters the estimated CNR. (a) DAS. (b) S-curve. (c) S-DAS.

A. Estimation of P$_{max}$

We aim to estimate the maximum probability of success, $P_{\max}$, in the context of lesion detection. For conciseness, let us call pathological pixels those that are part of the lesion (i.e., inside) and healthy pixels those that are not (i.e., outside).

Let us denote the image value at any given pixel as x, also known as the pixel value. The pixel value x can convey any kind of information and be expressed in any units, such as signal power, dB intensity, coherence, and speed of sound.

Let us define the probability density function of the values taken by the pathological pixels as $p_i(x)$ and the probability density function of the values taken by healthy pixels as $p_o(x)$.

Here, we concentrate on hypoechoic lesions that have been historically used to study lesion detectability. Hence, we consider that a pixel is detected if its value x is below a given threshold ϵ.

Let us define the probability of false detection $P_F(\epsilon)$ as the proportion of healthy pixels that are detected using a binary classifier with threshold ϵ and the probability of miss $P_M(\epsilon)$ as the proportion of pathological pixels that go undetected using the same threshold. These two probabilities can be computed from $p_i(x)$ and $p_o(x)$, as

$$P_F(\epsilon) = \int_{-\infty}^{\epsilon} p_o(x)\, dx \tag{9}$$

$$P_M(\epsilon) = \int_{\epsilon}^{\infty} p_i(x)\, dx. \tag{10}$$

The probability of error P_e can be calculated using the Bayesian paradigm

$$P_e(\epsilon) = P_o P_F(\epsilon) + P_i P_M(\epsilon) \tag{11}$$

where P_o and P_i are prior probabilities that are assigned based on the size of the regions of interest. For simplicity, we assume that both regions have the same area. Hence, $P_o = P_i = 0.5$ and

$$P_e(\epsilon) = \frac{P_F(\epsilon) + P_M(\epsilon)}{2}. \tag{12}$$

It is possible to find an optimal threshold ϵ_0 that minimizes $P_e(\epsilon)$, as shown in Fig. 2. When that threshold is chosen,
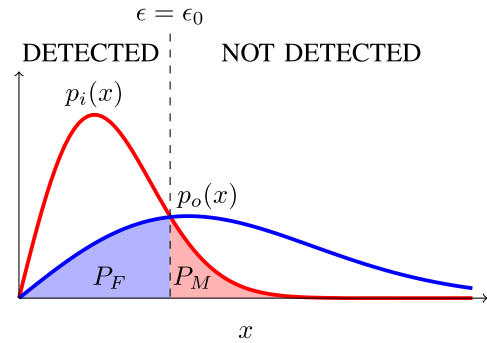

Fig. 2. Illustration of two probability density functions $p_i(x)$ and $p_o(x)$ and the resulting missclassification overlap $P_F(\epsilon)$ and $P_M(\epsilon)$ for an optimal threshold ϵ_0.

the binary classifier gives the minimum probability of error

$$P_{\min} = \min_{\epsilon}\{P_e(\epsilon)\}. \tag{13}$$

Combining (9) and (13), we see that

$$P_{\min} = \frac{1}{2}\left(\int_{-\infty}^{\epsilon_0} p_o(x)dx + \int_{\epsilon_0}^{\infty} p_i(x)\, dx\right) \tag{14}$$

which is equivalent to

$$P_{\min} = \frac{1}{2}\int_{-\infty}^{\infty} \min_{x}\{p_o(x), p_i(x)\}\, dx. \tag{15}$$

The integral in (15) is the overlap area between both the probability density functions (OVL), and hence

$$P_{\min} = \frac{\text{OVL}}{2} \tag{16}$$

and $P_{\max} = 1 - P_{\min}$ is, therefore

$$P_{\max} = 1 - \frac{\text{OVL}}{2}. \tag{17}$$

If both $p_i(x)$ and $p_o(x)$ overlap completely, OVL = 1 and $P_{\max} = 0.5$. This corresponds to the worst possible classification. If $p_i(x)$ and $p_o(x)$ do not overlap at all, then OVL = 0 and $P_{\max} = 1$.

The derivation presented here is valid for binary classifiers using a single threshold. However, OVL is a good estimator

of $P_{\min}$ even for multimodal distributions, where a set of thresholds must be used instead of a single one. For the case of hyperechoic lesions, the derivation is analogous and yields the same expression for (16).

B. Lesion Detectability

Even though $P_{\max}$ conveys all the information needed to evaluate the detection ability of any imaging algorithm, our field has long relied on contrast to measure lesion detectability. It may be convenient to generalize CNR so that it can be applied to distributions other than the circularly symmetric Normal distribution $\mathcal{CN}(0, \Gamma)$.

The classic CNR in (5), if applied on images generated with DAS, has two convenient properties.

1) CNR is correlated with $P_{\max}$.
2) CNR is bounded to the interval [0, 1].

Fulfilling these two properties, we define the gCNR as

$$\text{gCNR} = 2P_{\max} - 1 \qquad (18)$$

which can be written in terms of OVL as

$$\text{gCNR} = 1 - \text{OVL}. \qquad (19)$$

Notice that gCNR $= 0$, if $p_i(x)$ and $p_o(x)$ overlap completely (OVL$=1$, $P_{\max} = 0.5$), and gCNR $= 1$, if they do not overlap at all (OVL$=0$, $P_{\max} = 1$). gCNR is always proportional to $P_{\max}$, regardless of the distribution of the signals.

Furthermore, we argue that gCNR, rather than $P_{\max}$, constitutes a definition of what has been commonly referred to as lesion detectability [1], [13], [23]. gCNR measures how successful an ideal observer would be at the task of separating between healthy and pathological pixels.

If all pixels are classified as pathological, then gCNR $= 0$, which conveys the information that lesion detectability is zero and that the detection image holds no useful information. The same applies to the case where all the pixels are classified as healthy. If all pixels are correctly classified, then gCNR $= 1$, which conveys the idea that a perfect detection of the lesion is achieved and that the detection image is 100% accurate.

C. Analytical Expressions for DAS

Historically, anechoic cyst phantoms have been used to estimate contrast improvements. Said phantoms are composed of a background region with uniform, fully developed speckle, and an anechoic region. Uncorrelated bandpass noise is often added to the channel data to simulate different signal-to-noise ratio (SNR) conditions.

Interestingly, both speckle signal and thermal noise follow a circularly symmetric Normal distribution $\mathcal{CN}(0, \Gamma)$ if they are beamformed using DAS [14]. This means that the signal envelope is Rayleigh distributed and that the mean signal power follows an exponential distribution. Equivalently, this means that the real and imaginary parts of the demodulated signal are normally distributed.

Under these circumstances, it is possible to derive analytical expressions for C, CNR, and gCNR for any linear combination

of the signals across the aperture. Here, we will derive those expressions for DAS using a uniform flat aperture. Hereinafter, we assume that the lesion is anechoic and that thermal noise is present all over the image.

We start by defining the channel SNR as the power ratio

$$\text{SNR}_1 = \frac{v_S}{v_N} \qquad (20)$$

where v_S is the mean power of the speckle signal in one channel and v_N is the mean power of the uncorrelated noise in one channel. For simplicity, we assume that M elements are used on transmit and that the same number of elements are combined on receive. The SNR after combining the signal of M elements, for $M \gg 1$, is then

$$\text{SNR}_M = \frac{\mu_S}{\mu_N} = \frac{2/3 M^2 v_S}{M v_N} = \frac{2M}{3} \text{SNR}_1 \qquad (21)$$

where μ_S is the mean power of the speckle signal and μ_N is the mean power of the noise signal. The derivation of (21) is included in Appendix VII for any number of transmit and receive elements.

If we neglect resolution effects and acoustic noise, we can assume that inside the lesion, only thermal noise will be present, while outside the lesion, both speckle signal and noise will be found. Since both signals follow $\mathcal{CN}(0, \Gamma)$, it is possible to calculate the mean signal power in both regions as

$$\mu_i = \mu_N \qquad (22)$$
$$\mu_o = \mu_S + \mu_N. \qquad (23)$$

1) Contrast of DAS: The contrast between both the regions is computed by inserting (22) and (23) into (1)

$$\text{C}_0 = \frac{\mu_i}{\mu_o} = \left(\frac{\mu_S}{\mu_N} + 1 \right)^{-1} \qquad (24)$$

and by inserting (21) into (24), it yields

$$\text{C}_0 = \frac{3}{2M \, \text{SNR}_1 + 3}. \qquad (25)$$

2) CNR of DAS: The sum of two signals that follow $\mathcal{CN}(0, \Gamma)$ will also follow a $\mathcal{CN}(0, \Gamma)$ distribution. Consequently, the mean signal power in both regions will follow an exponential distribution and $\sigma^2 = \mu^2$. Then, expressions (5) and (8) become equivalent, and CNR becomes

$$\text{CNR}_0 = \frac{|\text{C}_0 - 1|}{\sqrt{\text{C}_0^2 + 1}} \qquad (26)$$

which is bounded between [0,1].

3) Maximum Probability of Success of DAS: Since the signal power in both regions follows an exponential distribution, their probability density functions are given by

$$p_i(x) = \frac{1}{\mu_i} e^{-x/\mu_i} \qquad (27)$$

$$p_o(x) = \frac{1}{\mu_o} e^{-x/\mu_o} \qquad (28)$$

where x is, in this case, the mean signal power, and hence, it is bounded by the interval $[0, \infty)$. By inserting (27)
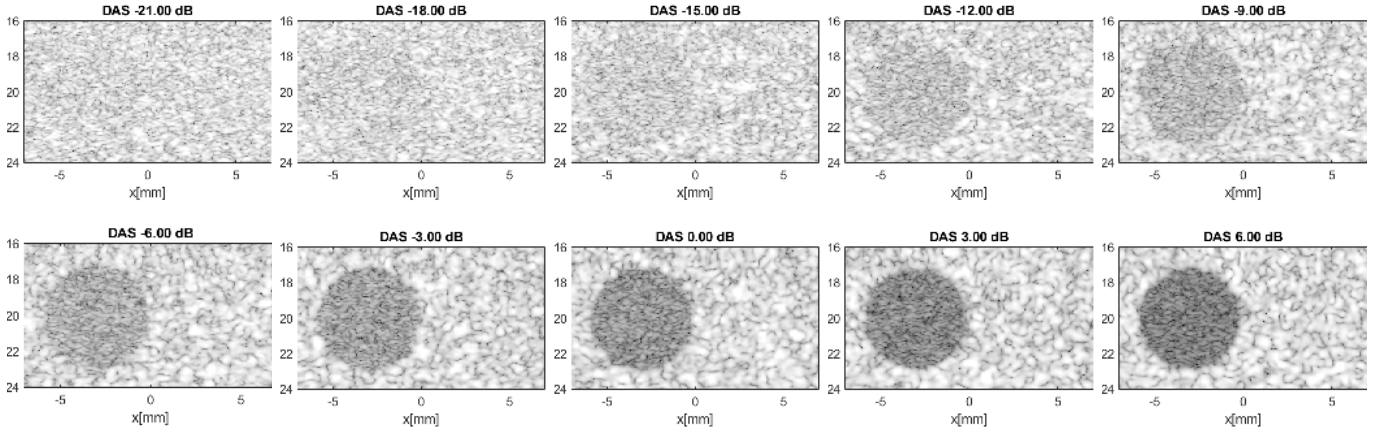
Fig. 3. B-mode images beamformed with DAS of ten of the *in silico* data sets used in this study for $SNR_1 \in [-21, 6]$ dB.

and (28) into (9) and (10), respectively, we obtain

$$P_F(\epsilon) = [-e^{-x/\mu_o}]_0^\epsilon = 1 - e^{-\epsilon/\mu_o} \tag{29}$$

$$P_M(\epsilon) = [-e^{-x/\mu_i}]_\epsilon^\infty = e^{-\epsilon/\mu_i}. \tag{30}$$

By inserting (29) and (30) into (12), we obtain the total probability of error

$$P_e(\epsilon) = \frac{1}{2} + \frac{1}{2}(e^{-\epsilon/\mu_i} - e^{-\epsilon/\mu_o}). \tag{31}$$

By differentiating (31), we find that it has a minimum at

$$\epsilon_0 = \frac{\mu_i \mu_o \ln(\mu_i/\mu_o)}{\mu_i - \mu_o}. \tag{32}$$

By substituting $\epsilon = \epsilon_0$ in (31), we obtain the minimum probability of error

$$P_{\min,0} = \frac{1}{2} + \frac{1}{2}\left[-C_0^{-\frac{C_0}{C_0-1}} + C_0^{-\frac{1}{C_0-1}} \right] \tag{33}$$

and $P_{\max}$ as the complementary probability

$$P_{\max,0} = \frac{1}{2} + \frac{1}{2}\left[C_0^{-\frac{C_0}{C_0-1}} - C_0^{-\frac{1}{C_0-1}} \right]. \tag{34}$$

By solving (26) for C_0 and inserting it into (34), it is possible to express $P_{\max,0}$ in terms of CNR_0. By plotting the resulting expression for $CNR_0 \in [0, 1]$, it becomes obvious that $P_{\max,0}$ and CNR_0 are correlated.

4) gCNR of DAS: Finally, by inserting (34) into (18), we obtain

$$gCNR_0 = C_0^{-\frac{C_0}{C_0-1}} - C_0^{-\frac{1}{C_0-1}}. \tag{35}$$

This derivation can be extended to cysts with a defined intensity (i.e., hypoechoic rather than anechoic) by redefining (22) and (23) as the mean signal power in each region plus the mean noise power; however, from (26), the derivation will remain unchanged. It must be noted that the analytical expressions derived here are only valid if the signal in the regions under test is a combination of uniform, fully developed speckle, and the additive bandpass Gaussian noise. New expressions would be needed if the speckle amplitude follows a non-Rayleigh distribution, such as Rician [24] or Nakagami [25].

IV. METHODS

We used Field II [26], [27] to simulate a 3-mm-radius anechoic cyst at 20-mm depth. A 128-element, 300-μm pitch, linear array was used to transmit a 5.13-MHz, 60% relative bandwidth pulse. A synthetic transmit aperture imaging sequence (STAI) was used, and the RF channel data were acquired; 100 different simulations of the same phantom were computed using independent and identically distributed speckle realizations to take into account the effect of speckle variability. Bandpass uncorrelated noise following a $\mathcal{CN}(0, \Gamma)$ distribution was added with different intensity levels so as to simulate $SNR_1 \in [-21, 6]$ dB.

In vitro data were collected using the Verasonics Vantage 256 research scanner. A 128-element, 300-μm pitch, linear array (Verasonics L11) was used, transmitting at 5.13 MHz. The probe was set against a CIRS multipurpose phantom (Model 040GSE). A 4.5-mm-diameter anechoic cyst located at 16-mm depth was selected as the lesion. Several STAI data sets were recorded using different transmit voltages, ranging from 10 to 0.4 V, to simulate different SNR conditions.

For both simulated and *in vitro* data, $M = 45$ elements were used both on transmit and receive, yielding a transmit and receive aperture size of 13.5 mm and an F-number of $F = 1.48$ at the lesion depth. Fig. 3 shows ten of the *in silico* data sets using a gray scale with a 60-dB dynamic range where the white color is set to the 99th percentile in each image.

The use of gCNR is also illustrated *in vivo*. A focused beam data set was acquired with the Verasonics Vantage 256 research scanner. A 128-element, 300-μm pitch, linear array (Philips L7-4) was used, transmitting at 5.2 MHz. In this case, $M = 32$ elements were used on transmit, and a constant F-number $F = 1$ was used on receive. As a target, we selected a cross section of the common carotid artery on a healthy volunteer.

The derivation in Section III-C purposely leaves out the effect of resolution and lesion size, i.e., the effects that would complicate the analytical solutions, limiting its usefulness. To validate them, we select two regions (I and O) that avoid the edges of the cyst. We chose the full-width at half-maximum of a uniformly weighted DAS beamformer as the system resolution. The lateral resolution can then be approximated
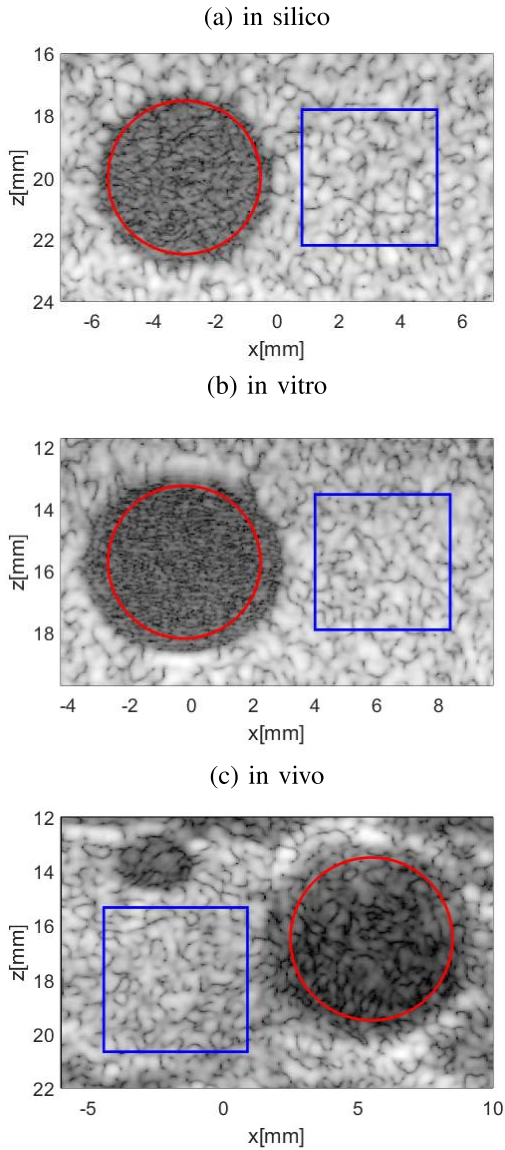
(a) in silico

(b) in vitro

(c) in vivo

Fig. 4. Two regions of interest I (inside red circle) and O (inside blue square) for (a) *in silico*, (b) *in vitro*, and (c) *in vivo* cases.

by $1.2\lambda F$ [28], resulting in a value of 0.53 mm. For both *in silico* and *in vitro* data, the inside region I is defined as the area inside the red circle in Fig. 4 with 2.47-mm radius. The outside region O is defined as the area within the blue square in Fig. 4 with sides of 4.378 mm. The areas of both regions are 19.17 mm^2. For the *in vivo* case, region I is enclosed by a 3-mm-radius circle, and region O is bounded by a 5.317-mm-side square, both having an area of 28.27 mm^2, as shown in Fig. 4(c).

The mean and standard deviation of the signal in both regions are estimated to compute the classic C and CNR. In order to calculate gCNR, the probability density functions in both regions are estimated by estimating the histogram over 100 bins covering the whole signal dynamic range. Fig. 5 shows the probability density function, inside and outside, of the signal envelope obtained for DAS and an SNR$_1$ = 0 dB.

We study C, CNR, and gCNR in seven imaging methods:

1) DAS;
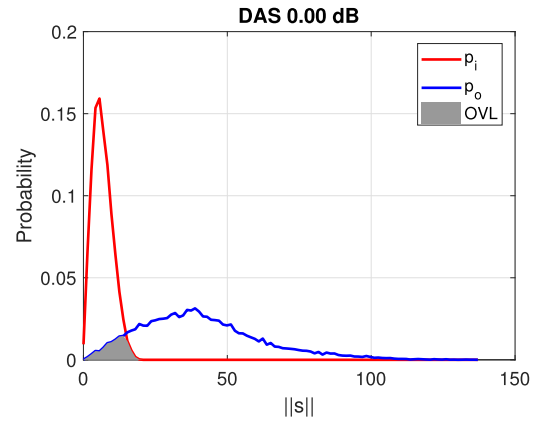2) DAS compressed with the S-curve in Fig. 1(b) (S-DAS);

Fig. 5. Estimated probability density function for the signal envelope of DAS for SNR$_1$ = 0 dB.

3) Mallart–Fink's coherence factor (CF) [3];
4) Camacho *et al.*'s phase CF (PCF) [5];
5) Li–Li's generalized CF (GCF) [21];
6) Matrone *et al.*'s delay-multiply-and-sum (DMAS) [29];
7) Lediju *et al.*'s SLSC [19].

Details of the implementation of each of the methods can be found in [2] and [19] and will, therefore, be omitted. For those methods with user settable parameters, we used $\gamma = 1$ for PCF, $M_0 = 4$ for GCF, and for SLSC a short-lag value $M_{max} = 14$ (denoted as M in [19]) and a kernel size of λ. All implementations are included in the UltraSound ToolBox [30] that can be download from http://www.ultrasoundtoolbox.com. The data sets used in this article and the scripts needed to reproduce the figures can be downloaded from http://www.ultrasoundtoolbox.com/publications/gcnr.

V. Results

Fig. 6 validates the analytical expressions (25), (26), and (35) against the estimation of C, CNR, and gCNR on simulated data using (1), (5), and (19). We see a good agreement between theory and simulation.

Fig. 7 shows the *in silico* B-mode images produced by all the tested methods for SNR$_1$ = 6 dB. Fig. 7 also shows the estimation of C, CNR, and gCNR for SNR$_1$ ∈ [−21, 6] dB. The analytical solutions for DAS are plotted as reference.

We observe that C and CNR vary significantly from method to method. S-DAS shows less contrast (C less negative) than DAS but higher CNR for SNR$_1$ > −10 dB. CF shows more contrast (C more negative) but significant lower CNR for SNR$_1$ ∈ [−15, 5] dB. GCF shows similar contrast to DAS but considerably higher CNR for SNR$_1$ > −5 dB. Both PCF and DMAS show more contrast (C more negative) than DAS but lower CNR. In general, we observe variations in CNR that range, approximately, from −50% to +250%.

This large variation is not present in gCNR. As expected, S-DAS has the same gCNR as DAS since it is a mere transformation of the dynamic range. Compared with DAS, the two methods, CF and PCF, show lower gCNR than DAS, with a maximum difference of -0.04 ± 0.01 at SNR$_1$ = 6 dB (CF) and -0.07 ± 0.03 at SNR$_1$ = −6 dB (PCF); the three
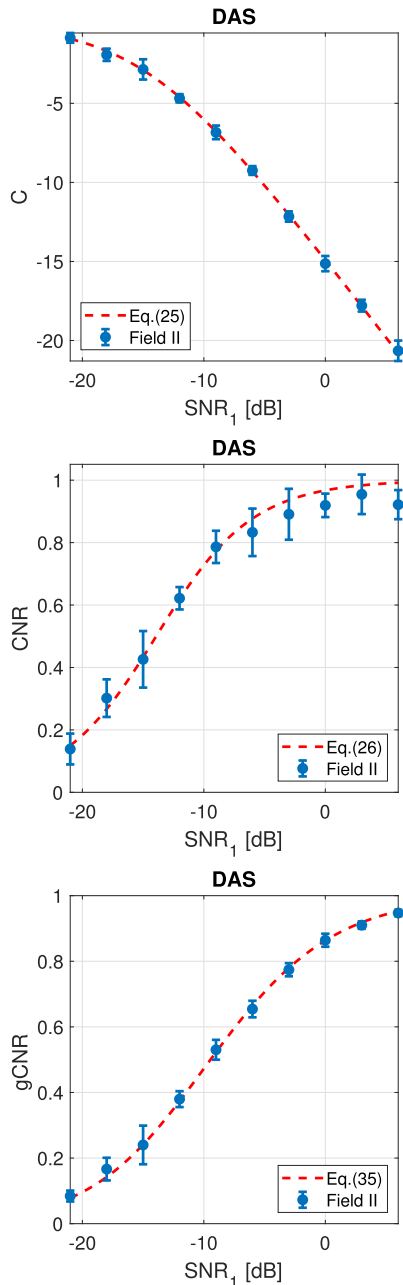
Fig. 6. *In silico* validation of expressions (25), (26), and (35).

methods, GCF, DMAS, and SLSC, show higher gCNR than DAS, with a maximum difference of 0.07 ± 0.02 at $\text{SNR}_1 = 0$ dB (GCF), 0.07 ± 0.03 for $\text{SNR}_1 = -6$ dB (DMAS), and 0.22 ± 0.03 at $\text{SNR}_1 = -6$ dB (SLSC).

The *in vitro* results are shown in Fig. 8. In this case, uncertainty intervals cannot be calculated as a single speckle realization is available. We observe a very good agreement between experimental data and (25), (26), and (35). As earlier, we observe a large variation between methods in C and CNR values, while the variation in gCNR is relatively small. As expected, S-DAS shows identical gCNR values to DAS. For the other tested techniques, we observe the same trend. CF and PCF show lower gCNR than DAS, with a maximum difference of -0.07 at $\text{SNR}_1 = 8.8$ dB (CF) and -0.08 for $\text{SNR}_1 = 8.8$ dB (PCF); GCF, DMAS, and SLSC show

higher gCNR than DAS, with a maximum difference of 0.10 for $\text{SNR}_1 = -5.2$ dB (GCF), 0.12 for $\text{SNR}_1 = -11.1$ dB (DMAS), and 0.29 for $\text{SNR}_1 = -11.1$ dB (SLSC).

The gCNR values plotted in Figs. 7 and 8 are included in Table I.

In Fig. 9, we illustrate the use of gCNR *in vivo*, using an image of the cross section of the common carotid artery. In this case, no noise is added to the data set, and hence, a single value is shown in Fig. 9 for each method and indices C, CNR, and gCNR.

As in previous scenarios, we observe a large variation in C and CNR between the methods. All methods show more contrast (C more negative) than DAS. In this case, most of the methods show smaller CNR than DAS, with the exception of S-DAS and SLSC that show, respectively, an increase of 37.6% and 74.5%.

As expected, the gCNR of S-DAS is almost identical to that of DAS. In this case, CF, PCF, and DMAS show lower gCNR than DAS, with variations of -0.108 (CF), -0.116 (PCF), and -0.049 (DMAS). GCF and SLSC show an increase in gCNR with variations of $+0.032$ (GCF) and $+0.049$ (SLSC).

VI. Discussion

By comparing the results of DAS and S-DAS, for various SNR conditions, we observe that DAS and S-DAS obtain equal gCNR values. This supports the hypothesis that gCNR is resistant to dynamic range transformations. We cannot argue that gCNR is immune to transformation because its result may change in case the transformation is noninjective, i.e., when two input values get the same output value. However, even in this case, the gCNR will never increase after transformation, which guarantees that gCNR cannot be spuriously increased due to dynamic range alteration.

The probability density functions, and hence, gCNR, can be computed on any kind of pixel data, regardless of their nature and physical meaning. This confirms the second hypothesis that gCNR can be used on a wide variety of imaging methods.

From (18), it is seen that gCNR is proportional to the maximum success rate $P_{\max}$, and hence, it conveys the same meaning. In addition, we argue that gCNR is a proper definition of lesion detectability, as the separability rate between healthy and pathological pixels. This way, a gCNR of 0.9 means that, at best, 90% of the pixels can be separated. This allows for a quantitative, meaningful comparison of imaging methods, which confirms our third hypothesis.

The gCNR metric can, therefore, be used to solve the methodological flaw of using C and CNR to measure contrast and properly compare the lesion detectability of different imaging methods.

The analytical expressions derived in Section III-C for DAS can serve as a sanity check for those aiming to benchmark different imaging algorithms. Said expressions are only valid for homogeneous, fully developed speckle. The alternative expression would be needed for other speckle models, such as Rician or Nakagami. However, it should be noted that gCNR remains an optimal separability test also for those distributions, as it imposes no condition on the probability density function of the signal.
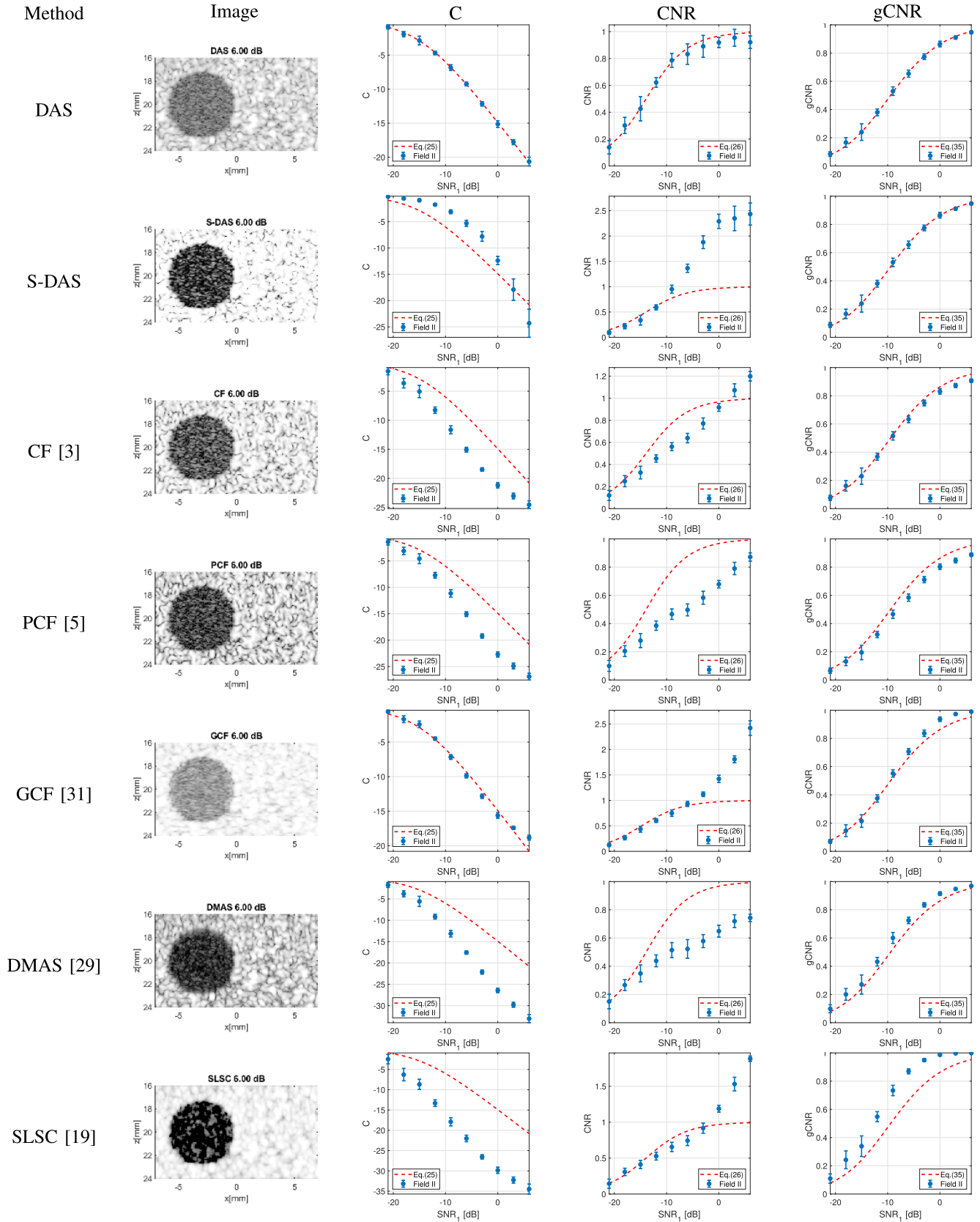
Fig. 7.   Comparison of the performance of C, CNR, and gCNR *in silico*.

The size of the regions of interest can have an impact on the estimation of gCNR. To obtain an accurate estimation of the PDF and, hence, of OVL, both regions should be large enough so as to contain multiple resolution cells, defined
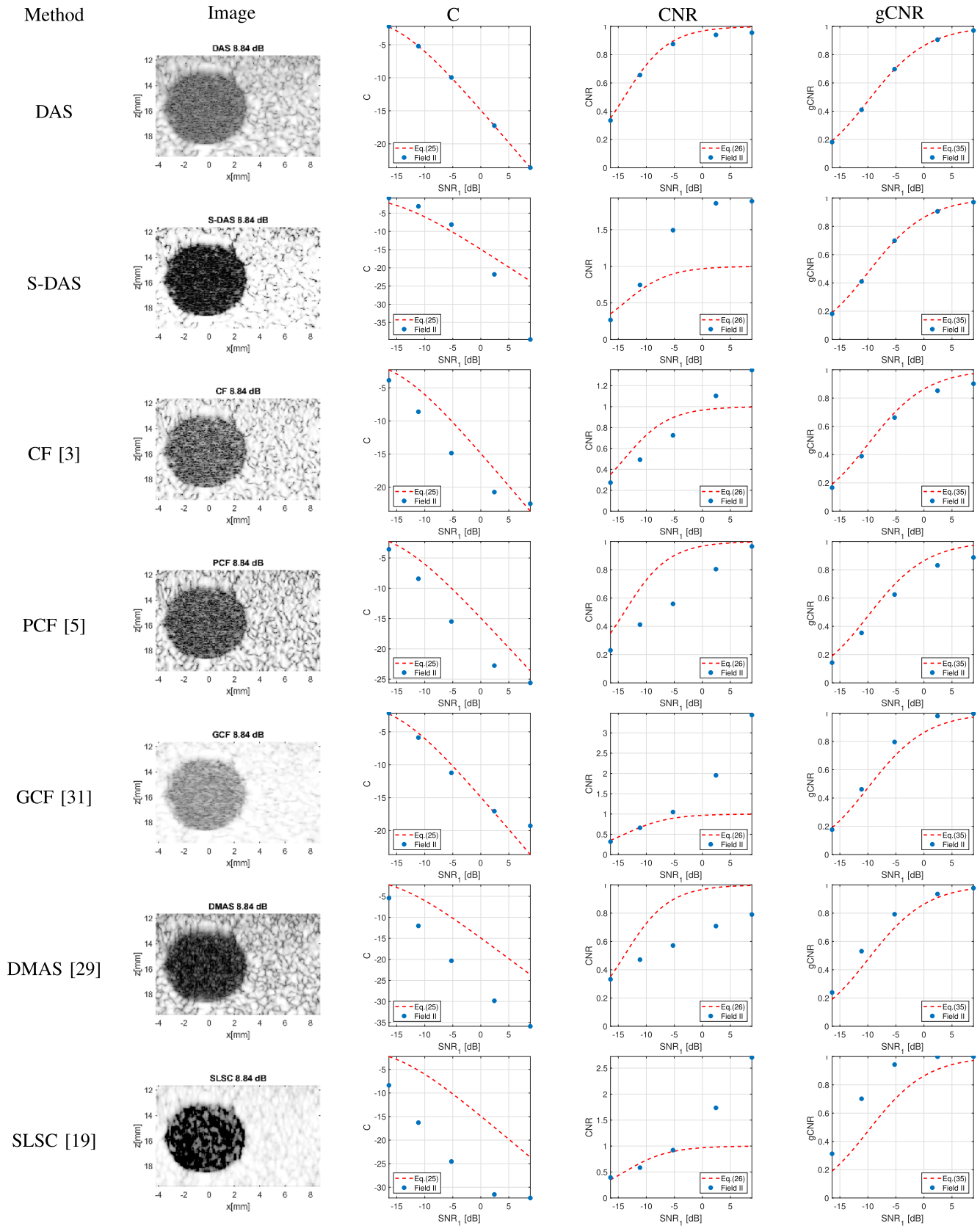
Fig. 8. Comparison of the performance of C, CNR, and gCNR *in vitro*.

as the -6-dB area of a single point scatterer. In the experiments presented here, the ROIs covered around 68 resolution cells, which was enough to produce an accurate estimation of gCNR. However, the impact of the spatial resolution on the estimation of gCNR must be studied further.
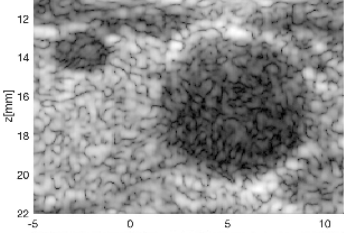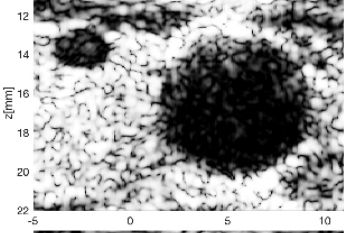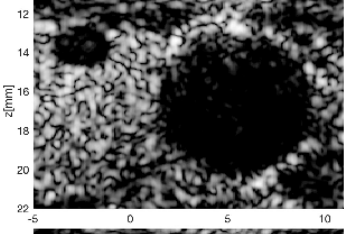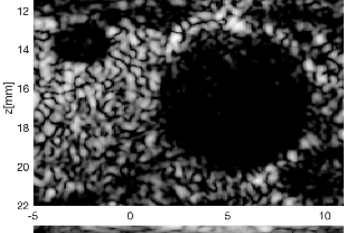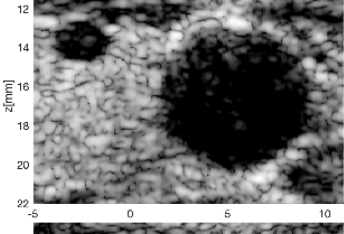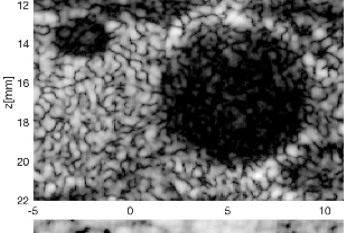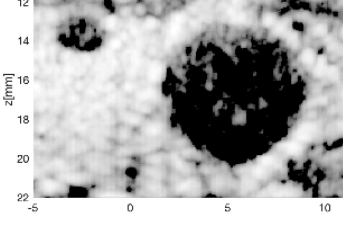
Method	Image	C	CNR	gCNR
DAS		-22.042	0.784	0.929
S-DAS		-36.203	1.080	0.934
CF [3]		-35.018	0.355	0.821
PCF [5]		-37.696	0.273	0.813
GCF [31]		-35.5742	0.574	0.961
DMAS [29]		-30.589	0.531	0.880
SLSC [19]		-29.809	1.369	0.975

Fig. 9. Comparison of the performance of C, CNR, and gCNR *in vivo*.

The comparison of the gCNR of state-of-the-art methods, *in silico* and *in vitro*, reveals that some methods (CF and PCF) worsen the probability of lesion detection with an absolute decrease in gCNR between −0.04 and −0.08. Other methods

	SNR$_1$ [dB]	DAS	S-DAS	CF [3]	PCF [5]	GCF [21]	DMAS [29]	SLSC [19]
in silico	-21	0.0842 ± 0.0167	0.0879 ± 0.0172	0.0763 ± 0.0183	0.0656 ± 0.0192	0.0708 ± 0.0134	0.0990 ± 0.0281	0.1096 ± 0.0329
	-18	0.1664 ± 0.0346	0.1662 ± 0.0331	0.1615 ± 0.0374	0.1316 ± 0.0297	0.1469 ± 0.0416	0.2004 ± 0.0415	0.2423 ± 0.0631
	-15	0.2400 ± 0.0589	0.2392 ± 0.0603	0.2304 ± 0.0579	0.1952 ± 0.0517	0.2144 ± 0.0445	0.2708 ± 0.0678	0.3390 ± 0.0730
	-12	0.3797 ± 0.0242	0.3801 ± 0.0240	0.3683 ± 0.0248	0.3223 ± 0.0226	0.3748 ± 0.0257	0.4321 ± 0.0303	0.5482 ± 0.0356
	-9	0.5301 ± 0.0302	0.5309 ± 0.0300	0.5157 ± 0.0294	0.4664 ± 0.0293	0.5521 ± 0.0260	0.6007 ± 0.0388	0.7337 ± 0.0367
	-6	0.6543 ± 0.0253	0.6559 ± 0.0255	0.6336 ± 0.0240	0.5840 ± 0.0258	0.7074 ± 0.0213	0.7248 ± 0.0226	0.8697 ± 0.0177
	-3	0.7742 ± 0.0200	0.7751 ± 0.0195	0.7486 ± 0.0199	0.7109 ± 0.0217	0.8364 ± 0.0229	0.8353 ± 0.0154	0.9492 ± 0.0113
	0	0.8642 ± 0.0199	0.8654 ± 0.0199	0.8311 ± 0.0190	0.8026 ± 0.0195	0.9365 ± 0.0158	0.9144 ± 0.0126	0.9864 ± 0.0057
	3	0.9102 ± 0.0113	0.9116 ± 0.0110	0.8724 ± 0.0146	0.8467 ± 0.0168	0.9730 ± 0.0069	0.9478 ± 0.0080	0.9968 ± 0.0018
	6	0.9471 ± 0.0097	0.9478 ± 0.0093	0.9066 ± 0.0115	0.8876 ± 0.0116	0.9895 ± 0.0047	0.9690 ± 0.0040	0.9989 ± 0.0014
in vitro	-16.4	0.1815	0.1819	0.1667	0.1430	0.1762	0.2390	0.3128
	-11.1	0.4097	0.4102	0.3889	0.3535	0.4616	0.5309	0.7017
	-5.2	0.6976	0.6986	0.6618	0.6247	0.7962	0.7923	0.9434
	2.4	0.9055	0.9061	0.8520	0.8310	0.9802	0.9353	0.9992
	8.8	0.9708	0.9710	0.9012	0.8869	0.9968	0.9774	1.0000

(GCF and DMAS) improve it slightly with an absolute increase between 0.07 and 0.12. One of the tested methods (SLSC) produced a relevant increase in detection probability with an absolute increase in gCNR between 0.22 and 0.29, meaning that an optimal observer would be able to separate between 22% and 29% more of the total number of pixels using this method than by using DAS.

The use of gCNR was also illustrated on an *in vivo* data set. The result followed the same general trend, with GCF and SLSC showing higher gCNR than DAS. Numerical values cannot be compared across scenarios since, in this case, the SNR is unknown. Comparison is also hindered by the presence of reverberation noise and the possibility of different speckle distributions. Even though the performance of different methods can vary between scenarios, gCNR remains a separability test even under those conditions.

It must be noted that the implementation of the state-of-the-art methods used here may not be specifically tuned to the problem of lesion detection. It is not the aim of this article to provide a benchmark of current beamforming technology but to propose the tools to do so.

The tested algorithms may not be particularly suited to the task of detecting cyst-like lesions. There is evidence showing that coherence-based methods may be better suited to improve the visualization of highly coherent echoes, such as delineation of tissue interfaces [32], microcalcifications [22], or solid content in hypoechoic lesions [33]. The problem of detecting uniform, purely scattering cysts may be better solved by speckle reduction techniques, such as spatial and frequency compounding [34] or nonlocal means [35]. The fact that spuriously large C and CNR values have been obtained with coherence-based methods may have misled the community into thinking that coherence methods could be used to increase the probability of detection of uniform cysts. Our results seem to indicate that only one of the coherence-based methods resulted in a significant increase in the probability of lesion detection, and it is yet to be proven if that improvement may be due to secondary factors, such as an inherent spatial smoothing.

It should be stressed that the scope of the comparison presented here is limited to uniform cysts in speckle in the presence of bandpass uncorrelated noise. The detection of lesions in the presence of other types of noise or unwanted signals, which can appear *in vivo*, remains to be investigated.

It must be noted that gCNR cannot be the only quality metric. Simply, by spatial smoothing, one can get a significant increase in gCNR, much greater than those obtained by the methods tested here. This, of course, makes sense; spatial smoothing reduces the variance of the probability density functions $p_i(x)$ and $p_o(x)$ and makes separation easier. There is, therefore, a tradeoff between spatial resolution and lesion detectability. Obtaining a high gCNR with low spatial resolution can be trivial. Both gCNR and spatial resolution must be studied simultaneously to assess the significance of any image formation algorithm.

VII. CONCLUSION

We present a new image quality metric, the gCNR, which is resistant to dynamic range alterations. gCNR can be estimated on all kind of images, regardless of compression, scale, or output units. We show that gCNR is a measure of lesion detectability as it measures the success rate of an optimal detector at the task of separating between healthy and pathological pixels.

This metric solves the methodological flaw of using the classic C and CNR with algorithms that alter the probability density function of ultrasound signals. However, by using gCNR alone, one cannot assess the significance of new imaging techniques. The spatial resolution must be also assessed to take account of trivial spatial averaging. Other metrics can also be included, such as the recently proposed lag-one coherence [36].

The imaginary border that separated the disciplines of beamforming and image processing is bound to disappear. We live in an era in which algorithms could be more advanced than our understanding of how they work. We must face the possibility that some data-driven algorithms may work just by finding loopholes in our experimental method and improve the tools we use to measure scientific relevance.
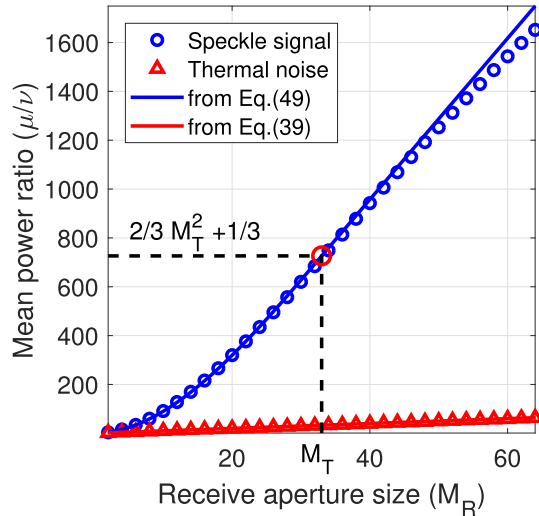
Fig. 10. *In silico* validation of (39) and (49).

APPENDIX
MEAN POWER OF SPECKLE SIGNAL AND THERMAL NOISE AFTER BEAMFORMING

Pieces of this derivation can be found in [3] and [36]. We include it here for convenience, and we expand the derivation for different aperture sizes both on transmit and receive.

Let us assume we have a linear array and that M_T active elements have been used to transmit an ultrasonic pulse using a uniform apodization ($=1$). Let us assume that M_R elements are combined on receive, also with uniform apodization. Let us assume that the pulse is optimally focused in all the beamformed pixels.

After demodulation, both speckle signal and thermal noise follow a circularly symmetric normal distribution, and hence, both its real and imaginary parts are normally distributed. Let us denote γ_S as the variance of the real and imaginary parts of the speckle signal and γ_N as the variance of the real and imaginary parts of the thermal noise.

The mean signal power follows an exponential distribution, whose probability density functions, for both speckle and noise, are

$$p_S(x) = \frac{1}{v_S} e^{-x/v_S} \qquad (36)$$

$$p_N(x) = \frac{1}{v_N} e^{-x/v_N} \qquad (37)$$

where $v_S = 2\gamma_S$ and $v_N = 2\gamma_N$ are, respectively, the mean signal power and mean noise power, in any of the elements.

The aim of this section is to derive the mean power of speckle signal μ_S and thermal noise μ_N after the combination of the signals received by M_R elements. As an intermediate step, we will calculate the variance of the real and imaginary parts of the speckle signal Γ_S and thermal noise Γ_N.

Hereinafter, we will use the symbol N_m to denote the thermal noise picked up by element m and S_m to denote the speckle signal received by the element m.

A. Thermal Noise

The thermal noise is independent and identically distributed in all the elements in the aperture, meaning that after beamformation, the real and imaginary parts of the thermal noise will be normally distributed with mean zero and variance

$$\Gamma_N = \mathrm{Var}\left(\sum_{m=1}^{M_R} N_m \right) = M_R \, \gamma_N. \qquad (38)$$

The mean power of the beamformed noise will then be

$$\mu_N = 2\,\Gamma_N = 2\,M_R\,\gamma_N = M_R\,v_N. \qquad (39)$$

In other words, after beamformation, the mean power of thermal noise increases linearly with the number of elements.

B. Speckle Signal

The speckle signal received by all elements is identically distributed, but it will be partially correlated along the aperture. Being circularly symmetric distributed, the mean of both the real and imaginary parts will be zero, and their variance will be given by sum of the covariances

$$\Gamma_S = \mathrm{Var}\left(\sum_{m=1}^{M_R} S_m \right) = \sum_{m=1}^{M_R} \sum_{n=1}^{M_R} \mathrm{Cov}(S_m, S_n) \qquad (40)$$

which is equivalent to

$$\Gamma_S = M_R \gamma_S + 2 \sum_{m=1}^{M_R} \sum_{n=m+1}^{M_R} \mathrm{Cov}(S_m, S_n). \qquad (41)$$

Since all channels have identical variance, γ_S can be taken out of the covariance calculation and

$$\Gamma_S = M_R \, \gamma_S + 2 \, \gamma_S \sum_{m=1}^{M_R} \sum_{n=m+1}^{M_R} R\,(S_m, S_n) \qquad (42)$$

where R denotes the correlation coefficient. The van Cittert–Zernike theorem [3] states that the correlation coefficient of speckle signal is given by

$$R(|n - m|, M_T) = \begin{cases} 1 - \dfrac{|n - m|}{M_T}, & \text{if } |n - m| < M_T \\ 0, & \text{otherwise.} \end{cases} \qquad (43)$$

Inserting (43) into (42), we obtain

$$\Gamma_S = M_R \, \gamma_S + 2 \, \gamma_S \sum_{m=1}^{M_R} \sum_{n=m+1}^{M_R} R\,(|n - m|, M_T). \qquad (44)$$

For the case $M_R < M_T$, the series in (44) has the solution shown in (45), as shown at the top of the next page. For $M_R \geq M_T$, the series in (44) can be written as the sum of the two series with the solution shown in (46), as shown at the top of the next page.

Inserting (45) and (46) into (44), we obtain

$$\Gamma_S = \gamma_S \Phi \qquad (47)$$

$$\sum_{m=1}^{M_R} \sum_{n=m+1}^{M_R} R(|n-m|, M_T) = \sum_{m=1}^{M_R} \sum_{n=m+1}^{M_R} \left(1 - \frac{|n-m|}{M_T}\right) = \frac{M_R}{6M_T}(1 - M_R)(M_R - 3M_T + 1) \tag{45}$$

$$\sum_{m=1}^{M_R} \sum_{n=m+1}^{M_R} R(|n-m|, M_T) = \sum_{m=1}^{M_R} \sum_{n=m+1}^{M_R} \left(1 - \frac{|n-m|}{M_T}\right) - \sum_{m=1}^{M_R - M_T} \sum_{n=m+M_T}^{M_R} \left(1 - \frac{|n-m|}{M_T}\right) = \frac{1}{6}(1 - M_T)(M_T - 3M_R + 1) \tag{46}$$

where

$$\Phi = \begin{cases} -\dfrac{M_R^3}{3M_T} + M_R^2 + \dfrac{M_R}{3M_T}, & \text{if } M_R < M_T \\ -\dfrac{M_T^2}{3} + M_T M_R + \dfrac{1}{3}, & \text{if } M_R \geq M_T. \end{cases} \tag{48}$$

The mean power of the speckle signal after beamformation is then

$$\mu_S = 2\Gamma_S = 2\Phi\gamma_S = \Phi\nu_S \tag{49}$$

where ν_S is the mean power of speckle noise for a single channel. The so-called beamformer gain of DAS is then given by the ratio of the SNR after and before beamforming

$$G = \frac{\mu_S/\mu_N}{\nu_S/\nu_N} = \frac{\Phi}{M_R}. \tag{50}$$

In particular, for the case of $M_R = M_T$, we find that

$$\mu_S = \left(\frac{2}{3}M_R^2 + \frac{1}{3}\right)\nu_S. \tag{51}$$

In other words, after beamformation, the mean power of the speckle signal increases quadratically with the number of elements.

In that case, the beamformer gain is

$$G = \frac{2}{3}M_R + \frac{1}{3\,M_R}. \tag{52}$$

For $M_R > 10$, these last two expressions can be approximated as

$$\mu_S \approx \frac{2}{3}M_R^2\nu_S \tag{53}$$

and

$$G \approx \frac{2}{3}M_R. \tag{54}$$

Fig. 10 shows an *in silico* validation of expressions (39) and (49), performed on data generated with Field II for a 128 elements λ pitch linear array transmitting at 5.2 MHz, for $M_T = 33$. We see that (49) slightly overestimates the mean power ratio μ_S/ν_S for $M_R > 40$, which was expected since (43) does not take into account the effect of element directivity.
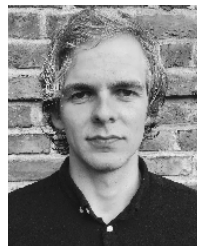
REFERENCES

[1] S. W. Smith, R. F. Wagner, J. M. Sandrik, and H. Lopez, "Low contrast detectability and contrast/detail analysis in medical ultrasound," *IEEE Trans. Sonics Ultrason.*, vol. SU-30, no. 3, pp. 164–173, May 1983.

[2] O. M. H. Rindal, A. Austeng, A. Fatemi, and A. Rodriguez-Molares, "The effect of dynamic range alterations in the estimation of contrast," *IEEE Trans. Ultrason., Ferroelectr., Freq. Control*, vol. 66, no. 7, pp. 1198–1208, Jul. 2019.

[3] R. Mallart and M. Fink, "Adaptive focusing in scattering media through sound-speed inhomogeneities: The van Cittert Zernike approach and focusing criterion," *J. Acoust. Soc. America*, vol. 96, no. 6, p. 3721, 1994.

[4] G. E. Trahey, S. W. Smith, and O. T. Von Ramm, "Speckle pattern correlation with lateral aperture translation: Experimental results and implications for spatial compounding," *IEEE Trans. Ultrason., Ferroelectr., Freq. Control*, vol. UFFC 33, no. 3, pp. 257–264, May 1986.

[5] J. Camacho, M. Parrilla, and C. Fritsch, "Phase coherence imaging," *IEEE Trans. Ultrason., Ferroelectr., Freq. Control*, vol. 56, no. 5, pp. 958–974, May 2009.

[6] J. Ophir, I. Céspedes, H. Ponnekanti, Y. Yazdi, and X. Li, "Elastography: A quantitative method for imaging the elasticity of biological tissues," *Ultrason. Imag.*, vol. 13, no. 2, pp. 111–134, Apr. 1991.

[7] M. Tanter and M. Fink, "Ultrafast imaging in biomedical ultrasound," *IEEE Trans. Ultrason., Ferroelectr., Freq. Control*, vol. 61, no. 1, pp. 102–119, Jan. 2014.

[8] M. Jaeger, E. Robinson, H. G. Akarçay, and M. Frenz, "Full correction for spatially distributed speed-of-sound in echo ultrasound based on measuring aberration delays via transmit beam steering," *Phys. Med. Biol.*, vol. 60, no. 11, pp. 4497–4515, May 2015. [Online]. Available: http://stacks.iop.org/0031-9155/60/i=11/a=4497

[9] M. Tanter *et al.*, "Quantitative assessment of breast lesion viscoelasticity: Initial clinical results using supersonic shear imaging," *Ultrasound Med. Biol.*, vol. 34, no. 9, pp. 1373–1386, Sep. 2008. [Online]. Available: http://www.ncbi.nlm.nih.gov/pubmed/18395961

[10] J. Kvam *et al.*, "Nonlinear elasticity imaging with dual frequency ultrasound," *J. Acoust. Soc. Amer.*, vol. 141, no. 5, p. 3719, 2017.

[11] A. Rodriguez-Molares, A. Fatemi, L. Løvstakken, and H. Torp, "Specular beamforming," *IEEE Trans. Ultrason., Ferroelectr., Freq. Control*, vol. 64, no. 9, pp. 1285–1297, Sep. 2017.

[12] M. S. Patterson and F. S. Foster, "The improvement and quantitative assessment of B-mode images produced by an annular array/cone hybrid," *Ultrason. Imag.*, vol. 5, no. 3, pp. 195–213, Jul. 1983.

[13] S. W. Smith, H. Lopez, and W. J. Bodine, "Frequency independent ultrasound contrast-detail analysis," *Ultrasound Med. Biol.*, vol. 11, no. 3, pp. 467–477, 1985. [Online]. Available: http://www.sciencedirect.com/science/article/pii/0301562985901589

[14] R. F. Wagner, S. W. Smith, J. M. Sandrik, and H. Lopez, "Statistics of speckle in ultrasound B-scans," *IEEE Trans. Sonics Ultrason.*, vol. SU-30, no. 3, pp. 156–163, May 1983.

[15] S. Mehdizadeh, A. Austeng, T. F. Johansen, and S. Holm, "Eigenspace based minimum variance beamforming applied to ultrasound imaging of acoustically hard tissues," *IEEE Trans. Med. Imag.*, vol. 31, no. 10, pp. 1912–1921, Oct. 2012.

[16] N. Q. Nguyen and R. W. Prager, "A Spatial coherence approach to minimum variance beamforming for plane-wave compounding," *IEEE Trans. Ultrason., Ferroelectr., Freq. Control*, vol. 65, no. 4, p. 522–534, Apr. 2018.

[17] J. Shin and L. Huang, "Spatial prediction filtering of acoustic clutter and random noise in medical ultrasound imaging," *IEEE Trans. Med. Imag.*, vol. 36, no. 2, pp. 396–406, Feb. 2017.

[18] S. Krishnan, K. W. Rigby, and M. O'Donnell, "Improved estimation of phase aberration profiles," *IEEE Trans. Ultrason., Ferroelectr., Freq. Control*, vol. 44, no. 3, pp. 701–713, May 1997.

[19] M. A. Lediju, G. E. Trahey, B. C. Byram, and J. J. Dahl, "Short-lag spatial coherence of backscattered echoes: Imaging characteristics," *IEEE Trans. Ultrason., Ferroelectr., Freq. Control*, vol. 58, no. 7, pp. 1377–1388, Jul. 2011.

[20] M. A. Lediju Bell, R. Goswami, J. A. Kisslo, J. J. Dahl, and G. E. Trahey, "Short-lag spatial coherence imaging of cardiac ultrasound data: Initial clinical results," *Ultrasound Med. Biol.*, vol. 39, no. 10, pp. 1861–1874, 2013. [Online]. Available: http://www.ncbi.nlm.nih.gov/pmc/articles/PMC3966558/

[21] P. C. Li and M. L. Li, "Adaptive imaging using the generalized coherence factor," *IEEE Trans. Ultrason., Ferroelectr., Freq. Control*, vol. 50, no. 2, pp. 128–141, Feb. 2003.

[22] S. M. Hverven, O. M. H. Rindal, A. J. Hunter, and A. Austeng, "Point scatterer enhancement in ultrasound by wavelet coefficient shrinkage," in *Proc. IEEE Int. Ultrason. Symp. (IUS)*, Sep. 2017, pp. 1–4.

[23] J. J. Dahl, D. Hyun, M. Lediju, and G. E. Trahey, "Lesion detectability in diagnostic ultrasound with short-lag spatial coherence imaging," *Ultrason. Imag.*, vol. 33, no. 2, pp. 119–133, 2011.

[24] M. F. Insana, R. F. Wagner, B. S. Garra, D. G. Brown, and T. H. Shawker, "Analysis of ultrasound image texture via generalized rician statistics," *Opt. Eng.*, vol. 25, no. 6, 1986, Art. no. 256743, doi: 10.1117/12.7973900.

[25] P. M. Shankar, "Ultrasonic tissue characterization using a generalized nakagami model," *IEEE Trans. Ultrason., Ferroelectr., Freq. Control*, vol. 48, no. 6, pp. 1716–1720, Nov. 2001.

[26] J. A. Jensen and N. B. Svendsen, "Calculation of pressure fields from arbitrarily shaped, apodized, and excited ultrasound transducers," *IEEE Trans. Ultrason., Ferroelectr., Freq. Control*, vol. 39, no. 2, pp. 262–267, Mar. 1992.

[27] J. A. Jensen, "FIELD: A program for simulating ultrasound systems," in *Proc. 10th Nordicbaltic Conf. Biomed. Imag.*, vol. 4, 1996, pp. 351–353.

[28] I. J. Harris, "On the use of windows for harmonic analysis with the discrete Fourier transform," *Proc. IEEE*, vol. 66, no. 1, pp. 51–83, Jan. 1978.

[29] G. Matrone, A. S. Savoia, and G. Magenes, "The delay multiply and sum beamforming algorithm in ultrasound B-mode medical imaging," *IEEE Trans. Med. Imag.*, vol. 34, no. 4, pp. 940–949, Apr. 2015.

[30] A. Rodriguez-Molares *et al.*, "The ultrasound toolbox," in *Proc. IEEE Int. Ultrason. Symp. (IUS)*, Sep. 2017, pp. 1–4.

[31] J. Li, P. Stoica, and Z. Wang, "On robust capon beamforming and diagonal loading," *IEEE Trans. Signal Process.*, vol. 51, no. 7, pp. 1702–1715, Jul. 2003.

[32] J. J. Dahl, M. Jakovljevic, G. F. Pinton, and G. E. Trahey, "Harmonic spatial coherence imaging: An ultrasonic imaging method based on backscatter coherence," *IEEE Trans. Ultrason., Ferroelectr., Freq. Control*, vol. 59, no. 4, pp. 648–659, Apr. 2012.

[33] A. Wiacek *et al.*, "Robust short-lag spatial coherence imaging of breast ultrasound data: Initial clinical results," *IEEE Trans. Ultrason., Ferroelectr., Freq. Control*, vol. 66, no. 3, pp. 527–540, Mar. 2019.

[34] J. Park, J. B. Kang, J. H. Chang, and Y. Yoo, "Speckle reduction techniques in medical ultrasound imaging," *Biomed. Eng. Lett.*, vol. 4, no. 1, pp. 32–40, Mar. 2014, doi: 10.1007/s13534-014-0122-6.

[35] L. H. Breivik, S. R. Snare, E. N. Steen, and A. H. S. Solberg, "Real-time nonlocal means-based despeckling," *IEEE Trans. Ultrason., Ferroelectr., Freq. Control*, vol. 64, no. 6, pp. 959–977, Jun. 2017.

[36] W. Long, N. Bottenus, and G. E. Trahey, "Lag-one coherence as a metric for ultrasonic image quality," *IEEE Trans. Ultrason., Ferroelectr., Freq. Control*, vol. 65, no. 10, pp. 1768–1780, Oct. 2018.

Ole Marius Hoel Rindal (S'14) was born in Hamar, Norway, in 1990. He received the M.S. degree in computer science (signal processing) and the Ph.D. degree in medical ultrasound beamforming techniques from the University of Oslo, Oslo, Norway, in 2014 and 2019, respectively.

He holds a postdoctoral position at the Department of Informatics, University of Oslo. He also holds a position at SINTEF, Trondheim, Norway, where he has been working with biomedical technology. His research interests are within medical ultrasound imaging, especially improving and evaluating the image quality resulting from beamforming techniques.

Jan D'hooge (M'98) was born in Sint-Niklaas, Belgium, in 1972. He received the M.Sc. and Ph.D. degrees in physics from the University of Leuven, Leuven, Belgium, in 1994 and 1999, respectively.

He was a Postdoctoral Researcher with the Medical Imaging Computing Laboratory, Electrical Engineering Department, University of Leuven, where he became acquainted with general problems in medical imaging, such as elastic registration, segmentation, shape analysis, and data acquisition problems related to other modalities (in particular, MRI). In 2006, he was appointed as an Associate Professor at the Department of Cardiovascular Sciences, Medical Faculty, University of Leuven. Since 2009, he has been a part-time Visiting Researcher with the Norwegian Institute of Science and Technology, Trondheim, Norway. He has authored or coauthored over 290 peer-reviewed articles, has contributed to 14 books, and has coedited two books. His current research interests include myocardial tissue characterization, deformation imaging, and cardiac pathophysiology.

Dr. D'hooge was an elected AdCom Member of the IEEE-UFFC Society from 2010 to 2012. He is also a member of the Acoustical Society of America and the European Association of Echocardiography. In 1999, he received the Young Investigator Award of the Belgian Society of Echocardiography. In 2000, he was nominated for the Young Investigator Award of the European Society of Echocardiography. He was the Chair of the Ultrasound Conference of the SPIE Medical Imaging Symposium from 2008 to 2011 and the Technical Vice-Chair of the IEEE Ultrasonics Symposium from 2008 to 2012 and its Technical Chair in 2014 and 2018. Since 2019, he has been the Chair of the IEEE Ultrasonics Symposium Guidance Committee.

Alfonso Rodriguez-Molares was born in A Coruña, Spain, in 1980. He received the M.Sc. degree in telecommunications and the Ph.D. degree in signal processing and communication from the University of Vigo, Vigo, Spain, in 2006 and 2011, respectively.

In 2012, as a Postdoctoral Researcher with the School of Mechanical Engineering, The University of Adelaide, Adelaide, SA, USA, he became interested in ultrasound imaging and acoustic propagation in heterogeneous media. In the Department of Circulation and Medical Imaging, Norwegian University of Science and Technology, Trondheim, Norway, he specialized in advanced beamforming and ultrasound image quality; first as a Postdoctoral Researcher from 2014 and later as a Senior Engineer from 2015. In 2019, he was appointed as an Assistant Professor at the Defense University Center, University of Vigo. He has coauthored over 20 articles in peer-reviewed journals. He holds two patents. His current research interests include medical ultrasound, adaptive beamforming, and underwater acoustics.

Svein-Erik Måsøy (M'07) was born in Halden, Norway, in 1975. He received the M.Sc. degree in applied mechanics, thermodynamics, and fluid dynamics and the Ph.D. degree from the Norwegian University of Science and Technology (NTNU), Trondheim, Norway, in 1999 and 2004, respectively. His Ph.D. dissertation entitled Estimation and Correction of Aberration in Medical Ultrasound Imaging.

He is currently a Researcher with the Department of Circulation and Medical Imaging, NTNU. His current research interests are nonlinear acoustics, beamforming, machine learning, and nondestructive testing using ultrasound.

Andreas Austeng (S'97–M'01–SM'16) received the M.S. degree in physics and the Ph.D. degree in computer science from the University of Oslo, Oslo, Norway, in 1996 and in 2001, respectively.

Since 2001, he has been a Postdoctoral Research Fellow and an Associate Professor with the Department of Informatics, University of Oslo, where he is currently a Professor with the Digital Signal Processing and Image Analysis Group. His research interests include signal processing for acoustical imaging and algorithms that aim to improve the quality of information extracted from images.

Muyinatu A. Lediju Bell (S'08–M'14–SM'19) received the B.S. degree in mechanical engineering with a minor in biomedical engineering from the Massachusetts Institute of Technology, Cambridge, MA, USA, in 2006, and the Ph.D. degree in biomedical engineering from Duke University, Durham, NC, USA, in 2012.

From 2009 to 2010, she conducted research abroad as a Whitaker International Fellow at The Institute of Cancer Research and Royal Marsden Hospital, Surrey, U.K. From 2012 to 2016, she was a Postdoctoral Fellow with the Engineering Research Center for Computer-Integrated Surgical Systems and Technology, Johns Hopkins University, Baltimore, MD, USA. She is currently an Assistant Professor with the Department of Electrical and Computer Engineering with a joint appointment with the Department of Biomedical Engineering, Johns Hopkins University, where she founded and currently directs the Photoacoustic and Ultrasonic Systems Engineering Laboratory. Her research interests include ultrasound and photoacoustic imaging, coherence-based beamforming, image-guided surgery, robotics, and medical device design.

Dr. Bell received the NSF CAREER Award in 2018, the NIH Trailblazer Award in 2018, the MIT Technology Reviews Innovator Under 35 Award in 2016, and the NIH K99/R00 Pathway to Independence Award in 2015. She also serves as an Associate Editor for the IEEE TRANSACTIONS ON ULTRASONICS, FERROELECTRICS, AND FREQUENCY CONTROL.

Hans Torp (M'93) was born in Sarpsborg, Norway, in 1953. He received the M.S. and Dr.Techn. degrees from the University of Trondheim, Trondheim, Norway, in 1978 and 1992, respectively.

Since 1983, he has been with the Department of Circulation and Medical Imaging, Faculty of Medicine, Norwegian University of Science and Technology, Trondheim, where he has been a full-time Professor since 1998. His research interests include stochastic signal/image processing with applications in ultrasonic imaging, Doppler, and color flow imaging.